Exploring theoretical uncertainties in the hydrodynamic description of relativistic heavy-ion collisions

Cheng Chiu[1,*] and Chun Shen[2,3,†]

[1]*Cranbrook Kingswood Upper School, Bloomfield Hills, Michigan 48304, USA*

[2]*Department of Physics and Astronomy, Wayne State University, Detroit, Michigan 48201, USA*

[3]*RIKEN BNL Research Center, Brookhaven National Laboratory, Upton, New York 11973, USA*

(Received 22 March 2021; accepted 25 May 2021; published 2 June 2021)

We explore theoretical uncertainties in the hydrodynamic description of relativistic heavy-ion collisions by examining the full nonlinear causality conditions and quantifying the second-order transport coefficients' role on flow observables. The causality conditions impose physical constraints on the maximum allowed values of inverse Reynolds numbers during the hydrodynamic evolution. Including additional second-order gradient terms in the Denicol-Niemi-Molnár-Rischke (DNMR) theory significantly shrinks the casual regions compared to those in the Israel-Stewart hydrodynamics. For Au+Au collisions, we find the variations of flow observables are small with and without imposing the necessary causality conditions, suggesting a robust extraction of the quark-gluon plasma's transport coefficients in previous model-to-data comparisons. However, sizable sensitivity is present in small p+Au collisions, which poses challenges to study the small systems' collectivity.

DOI: 10.1103/PhysRevC.103.064901

I. INTRODUCTION

Relativistic viscous hydrodynamics has been the most successful model to provide a quantitative macroscopic description of heavy-ion collision dynamics at high energies [1–7]. It is an efficient and effective phenomenological framework to extract many-body properties of nuclear matter under extremely hot and dense conditions. As the QCD macroscopic properties emerge from the interactions among quarks and gluons, the quark-gluon plasma (QGP) transport coefficients can be extracted from the comparisons between the hydrodynamic modeling and experimental data [8–13]. Hydrodynamic simulations also provide detailed space-time evolution of relativistic heavy-ion collisions for studying the modification of rare probes under a hot nuclear environment, such as enhanced thermal electromagnetic radiation and suppression of QCD jets [14–21].

Most phenomenological simulations ensure causality on the linear level by choosing the relaxation times for the shear and bulk viscosity to be larger than the linear causality conditions [22–25]. These conditions are "static," i.e., the causality bounds purely depend on the transport coefficients as functions of temperature and chemical potentials. There were attempts to go beyond the linear regime in restricted in 1+1 dimensions or with strong symmetry conditions [26,27]. Recently, the full nonlinear causality conditions were derived in Ref. [28] for the Israel-Stewart (IS) and Denicol-Niemi-Molnár-Rischke (DNMR) theories [29–32]. These more robust causality conditions directly involve the dynamically evolved shear stress tensor and bulk viscous pressure. Therefore, the equation of motion of IS and DNMR hydrodynamics alone cannot guarantee that a system will always stay within the causality region during evolution. Causalilty conditions need to be examined locally in each fluid cell throughout the entire evolution.

The causality conditions can serve as physics constraints on the sizes of the shear stress tensor $\pi^{\mu\nu}$ and bulk viscous pressure Π. The constraints on their sizes were introduced as numerical regulators to stabilize the event-by-event numerical simulations [33–35]. The causality conditions provide us with useful theoretical guidance on these regulators' numerical choices in relativistic hydrodynamic simulations.

Recently, Bayesian inference techniques were applied to systematically constrain multiple model parameters with various experimental measurements [36–42]. The causality conditions can provide additional constraints on the prior ranges for the first- and second-order transport coefficients. At the same time, ensuring the full nonlinear causality conditions will reduce the theoretical uncertainty from the choices of numerical regulators in the hydrodynamic simulations.

In this work, we will systematically examine the full nonlinear causality conditions derived in Ref. [28] in event-by-event simulations of relativistic heavy-ion collisions. We will further quantify the role of additional second-order gradient terms in the DNMR theory on flow observables.

II. THE HYDRODYNAMIC FRAMEWORK

The hydrodynamic equations of motion for the collision system's stress-energy tensor represent the energy-momentum conservation as

$$\partial_\mu T^{\mu\nu} = 0\,. \tag{1}$$

*cchiu22@cranbrook.edu

†chunshen@wayne.edu

TABLE I. The choice of second-order transport coefficients used in the restricted and full DNMR hydrodynamic theories [48,50].

	Restricted DNMR with $\tau_{\Pi,1}$	Restricted DNMR with $\tau_{\Pi,2}$	DNMR with $\tau_{\Pi,1}$	DNMR with $\tau_{\Pi,2}$
$\frac{\eta}{\tau_\pi(\varepsilon+P)}=\frac{1}{C_\eta}$	$\frac{1}{5}$	$\frac{1}{5}$	$\frac{1}{5}$	$\frac{1}{5}$
$\frac{\zeta}{\tau_\Pi(\varepsilon+P)}=\frac{1}{C_\zeta}$	$14.55(\frac{1}{3}-c_s^2)^2$	$\frac{7}{C_\eta}(\frac{1}{3}-c_s^2)$	$14.55(\frac{1}{3}-c_s^2)^2$	$\frac{7}{C_\eta}(\frac{1}{3}-c_s^2)$
$\frac{\delta_{\pi\pi}}{\tau_\pi}$	$\frac{4}{3}$	$\frac{4}{3}$	$\frac{4}{3}$	$\frac{4}{3}$
$\frac{\delta_{\Pi\Pi}}{\tau_\Pi}$	$\frac{2}{3}$	$\frac{2}{3}$	$\frac{2}{3}$	$\frac{2}{3}$
$\frac{\tau_{\pi\pi}}{\tau_\pi}$	0	0	$\frac{10}{7}$	$\frac{10}{7}$
$\frac{\lambda_{\pi\Pi}}{\tau_\pi}$	0	0	$\frac{6}{5}$	$\frac{6}{5}$
$\frac{\lambda_{\Pi\pi}}{\tau_\Pi}$	0	0	$\frac{8}{5}(\frac{1}{3}-c_s^2)$	$\frac{8}{5}(\frac{1}{3}-c_s^2)$
φ_7	0	0	$\frac{9}{70}\frac{4}{\varepsilon+P}$	$\frac{9}{70}\frac{4}{\varepsilon+P}$

In the Israel-Stewart and the DNMR formalisms [29–32], the out-of-equilibrium shear stress tensor and bulk viscous pressure are treated as independent degrees of freedom, and they evolve with the following relaxation type of equations,

$$\tau_\Pi\dot{\Pi}+\Pi=-\zeta\,\theta-\delta_{\Pi\Pi}\Pi\,\theta+\lambda_{\Pi\pi}\pi^{\mu\nu}\sigma_{\mu\nu}, \tag{2}$$

$$\tau_\pi\dot{\pi}^{\langle\mu\nu\rangle}+\pi^{\mu\nu}=2\eta\,\sigma^{\mu\nu}-\delta_{\pi\pi}\pi^{\mu\nu}\theta+\varphi_7\pi_\alpha^{\langle\mu}\pi^{\nu\rangle\alpha},\\ -\tau_{\pi\pi}\pi_\alpha^{\langle\mu}\sigma^{\nu\rangle\alpha}+\lambda_{\pi\Pi}\Pi\,\sigma^{\mu\nu}. \tag{3}$$

Here $A^{\langle\cdots\rangle}$ denotes symmetrized and traceless projections, $\theta=\nabla_\mu u^\mu$ is the expansion rate, and

$$\sigma^{\mu\nu}=\tfrac{1}{2}\big[\nabla^\mu u^\nu+\nabla^\nu u^\mu-\tfrac{2}{3}\Delta^{\mu\nu}(\nabla_\alpha u^\alpha)\big] \tag{4}$$

is the velocity shear tensor, with $\nabla_\mu=(g_{\mu\nu}-u_\mu u_\nu)\partial^\nu$. The first-order transport coefficients η and ζ are the shear and bulk viscosity, respectively. The numerical values of all the other second-order transport coefficients $\{\tau_\pi,\tau_\Pi,\delta_{\Pi\Pi},\lambda_{\Pi\pi},\delta_{\pi\pi},\tau_{\pi\pi},\lambda_{\pi\Pi},\varphi_7\}$ are summarized in Table I.

The nonlinear causality conditions for the DNMR theory were derived in Ref. [28]. Here, we rewrite the causality inequality equations in terms of unitless ratios of the viscous pressure tensors over the enthalpy, $\varepsilon+P$. The nonzero eigenvalues of the shear stress tensor are denoted as $\{\Lambda_i\}(i=1,2,3)$. The traceless condition of the shear stress tensor requires $\Lambda_1+\Lambda_2+\Lambda_3=0$. We also define the unitless coefficients $C_\eta=\tau_\pi(\varepsilon+P)/\eta$ and $C_\zeta=\tau_\Pi(\varepsilon+P)/\zeta$ for the ratios of the shear and bulk relaxation times to the shear and bulk viscosity, respectively. The shear coefficient C_η is often approximated as a constant from 5–7 in kinetic theories [43,44] or $(4-2\ln 2)$ in the stronglycoupled theory [45,46]. In this work, we set $C_\eta=5$. The bulk coefficient $C_\zeta\propto 1/(1/3-c_s^2)^\alpha$ with $\alpha=1$ in the strongly coupled theory [47–49] and $\alpha=2$ from the kinetic approach [25,32,50]. In this work, we will examine hydrodynamic evolution with the following two choices for the bulk relaxation time:

$$\tau_{\Pi,1}=C_{\zeta,1}\frac{\zeta}{\varepsilon+P}=\frac{1}{14.55\big(1/3-c_s^2\big)^2}\frac{\zeta}{\varepsilon+P} \tag{5}$$

and

$$\tau_{\Pi,2}=C_{\zeta,2}\frac{\zeta}{\varepsilon+P}=\frac{C_\eta}{7\big(1/3-c_s^2\big)}\frac{\zeta}{\varepsilon+P}. \tag{6}$$

The first choice $\tau_{\Pi,1}$ was derived in kinetic theory [50] and was widely used in hydrodynamic simulations [12,35,36,38,40,51]. The parametric form of the second choice $\tau_{\Pi,2}$ is motivated from the strongly coupled theory [25,47,48].

According to Ref. [28] the necessary conditions for causality can be written as

$$n_1\equiv\frac{2}{C_\eta}+\frac{\lambda_{\pi\Pi}}{\tau_\pi}\frac{\Pi}{\varepsilon+P}-\frac{\tau_{\pi\pi}}{2\tau_\pi}\frac{|\Lambda_1|}{\varepsilon+P}\geqslant 0, \tag{7}$$

$$n_2\equiv 1-\frac{1}{C_\eta}+\left(1-\frac{\lambda_{\pi\Pi}}{2\tau_\pi}\right)\frac{\Pi}{\varepsilon+P}-\frac{\tau_{\pi\pi}}{4\tau_\pi}\frac{\Lambda_3}{\varepsilon+P}\geqslant 0, \tag{8}$$

$$n_3\equiv\frac{1}{C_\eta}+\frac{\lambda_{\pi\Pi}}{2\tau_\pi}\frac{\Pi}{\varepsilon+P}-\frac{\tau_{\pi\pi}}{4\tau_\pi}\frac{\Lambda_3}{\varepsilon+P}\geqslant 0, \tag{9}$$

$$n_4\equiv 1-\frac{1}{C_\eta}+\left(1-\frac{\lambda_{\pi\Pi}}{2\tau_\pi}\right)\frac{\Pi}{\varepsilon+P}+\left(1-\frac{\tau_{\pi\pi}}{4\tau_\pi}\right)\frac{\Lambda_a}{\varepsilon+P}-\frac{\tau_{\pi\pi}}{4\tau_\pi}\frac{\Lambda_d}{\varepsilon+P}\geqslant 0,\quad (a\neq d), \tag{10}$$

$$n_5\equiv c_s^2+\frac{4}{3}\frac{1}{C_\eta}+\frac{1}{C_\zeta}+\left(\frac{2}{3}\frac{\lambda_{\pi\Pi}}{\tau_\pi}+\frac{\delta_{\Pi\Pi}}{\tau_\Pi}+c_s^2\right)\frac{\Pi}{\varepsilon+P}+\left(\frac{3\delta_{\pi\pi}+\tau_{\pi\pi}}{3\tau_\pi}+\frac{\lambda_{\Pi\pi}}{\tau_\Pi}+c_s^2\right)\frac{\Lambda_1}{\varepsilon+P}\geqslant 0, \tag{11}$$

$$n_6\equiv 1-\left(c_s^2+\frac{4}{3}\frac{1}{C_\eta}+\frac{1}{C_\zeta}\right)+\left(1-\frac{2}{3}\frac{\lambda_{\pi\Pi}}{\tau_\pi}-\frac{\delta_{\Pi\Pi}}{\tau_\Pi}-c_s^2\right)\frac{\Pi}{\varepsilon+P}+\left(1-\frac{3\delta_{\pi\pi}+\tau_{\pi\pi}}{3\tau_\pi}-\frac{\lambda_{\Pi\pi}}{\tau_\Pi}-c_s^2\right)\frac{\Lambda_3}{\varepsilon+P}\geqslant 0. \tag{12}$$

The original necessary conditions n_5 and n_6 in Ref. [28] are simplified with the condition $(\frac{\delta_{\pi\pi}}{\tau_\pi}+\frac{\tau_{\pi\pi}}{3\tau_\pi}+\frac{\lambda_{\Pi\pi}}{\tau_\Pi}+c_s^2)>1$ in Eqs. (11) and (12) according to the values of second-order transport coefficients in Table I [50]. The sufficient causality conditions can be found in the Appendix. We first examine the causality constraints with different functional forms of C_ζ in the absence of viscous corrections, at which $\Pi=\Lambda_i=0$ $(i=1,2,3)$. In this case, both the necessary and sufficient

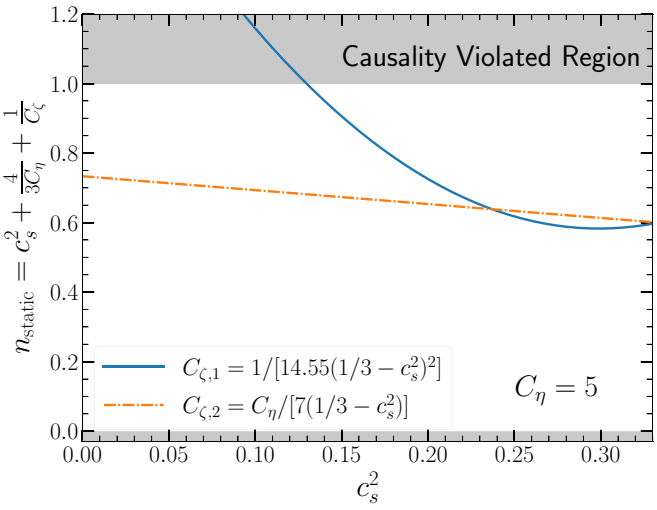

FIG. 1. The causal region for two choices of relaxation time of bulk viscosity as a function of the square of the speed of sound c_s^2 in the absence of viscous corrections, $\Pi = \Lambda_i = 0$ $(i = 1, 2, 3)$.

causality conditions reduce to

$$0 \leqslant n_{\rm static} \equiv c_s^2 + \frac{4}{3C_\eta} + \frac{1}{C_\zeta} \leqslant 1. \tag{13}$$

Figure 1 shows the value of $n_{\rm static}$ as a function of the speed of sound squared for the two choices of C_ζ. At the conformal limit c_s^2 goes to $1/3$, C_ζ approaches $+\infty$ and $n_{\rm static}$ approaches $(C_\eta + 4)/(3C_\eta) = 0.6$ when $C_\eta = 5$. The $C_{\zeta,1}$ from the kinetic theory with relaxation time approximation [50] has a quadratic dependence on c_s^2, which leads to a rapid increase of $n_{\rm static}$ at small c_s^2 values. With the coefficient 14.55 in $C_{\zeta,1}$, the $n_{\rm static}$ exceeds the causality bound for $c_s^2 < 0.13$. Although the minimum c_s^2 in the lattice QCD EoS at zero net baryon density is around 0.15 [shown in Fig. 2(a) below], this choice of $C_{\zeta,1}$ leads to a strong restriction on the sizes of the viscous stress tensor $\pi^{\mu\nu}$ and Π near the smooth crossover region where $c_s^2 \approx 0.15$. If the EoS has a soft point $c_s^2 \to 0$ at some finite baryon density, $C_{\zeta,1}$ will be ruled out by the causality conditions. To ensure $0 \leqslant n_{\rm static} \leqslant 1$ for $0 \leqslant c_s^2 \leqslant 1/3$, the quadratic c_s^2 parametrization requires the coefficient to be less than $9 - (12/C_\eta) = 6.6$ for $C_\eta = 5$. On the other hand, the strongly coupled theory suggests a linear dependence of c_s^2 in $1/C_\zeta$. Figure 1 shows that $n_{\rm static}$ with $C_{\zeta,2}$ increases much more slowly than that with $C_{\zeta,1}$.

Figure 2 shows the speed of sound squared from a lattice QCD EoS [52,53] and the transport coefficients that will be used to simulate relativistic heavy-ion collisions. We use the specific shear and bulk viscosity from Ref. [35]. The two choices of the bulk relaxation time τ_Π are shown in Fig. 2(c). We will examine event-by-event hydrodynamic simulations for Au+Au collisions and p+Au collisions at the top Relativistic Heavy Ion Collider (RHIC) energy. We expect a longer hydrodynamic phase at higher Large Hadron Collider (LHC) energies, which will reduce the flow observables' sensitivity to the choice of the bulk relaxation time compared to those at the RHIC.

Table I summarizes the numerical values of all the second-order transport coefficients that we will use in this

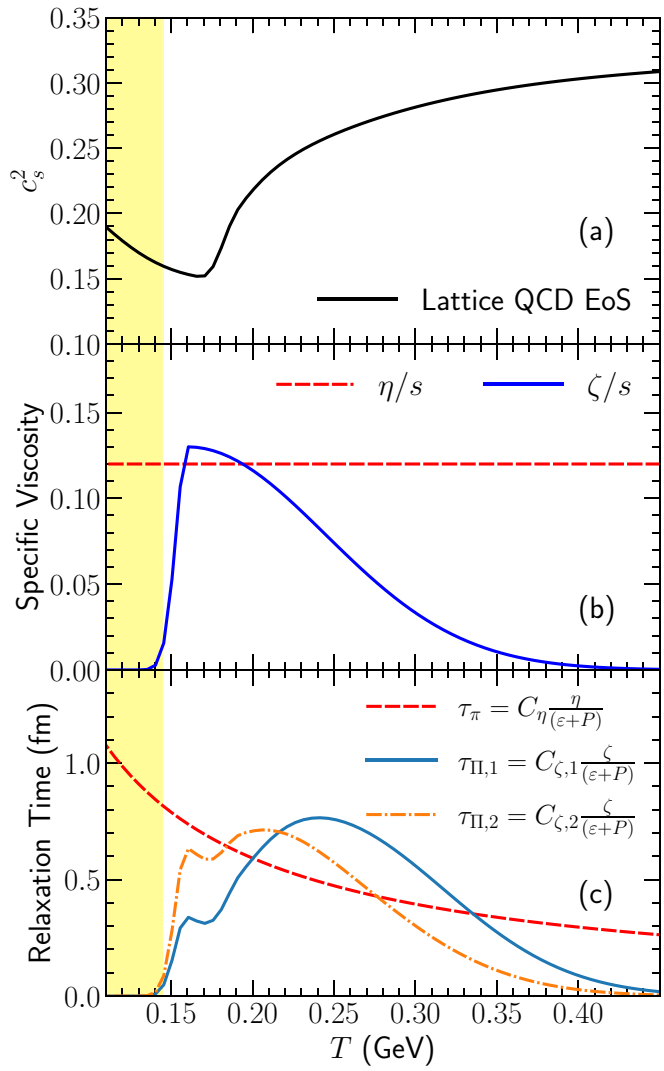

FIG. 2. (a) The square of the speed of sound from a lattice QCD–based EoS as a function of temperature. [(b), (c)] The specific shear and bulk viscosity and their relaxation times as functions of temperature used in this work. The region in yellow represents the phase ascribed to UrQMD in this work.

work. We refer to the simulations with nonzero values $\{\tau_{\pi\pi}, \lambda_{\pi\Pi}, \lambda_{\Pi\pi}, \varphi_7\}$ as the DNMR theory, while the restricted DNMR theory, which is close to the original Israel-Stewart hydrodynamics, only includes the relaxation times for shear and bulk viscosity and $\delta_{\pi\pi}$ and $\delta_{\Pi\Pi}$ terms in the equations of motion.

In hydrodynamic simulations, it is practical to track the evolution of the inverse Reynolds numbers for the shear stress tensor,

$$R_\pi \equiv \frac{\sqrt{\pi^{\mu\nu}\pi_{\mu\nu}}}{\varepsilon + P}, \tag{14}$$

and for the bulk viscous pressure,

$$R_\Pi \equiv \frac{\Pi}{\varepsilon + P}. \tag{15}$$

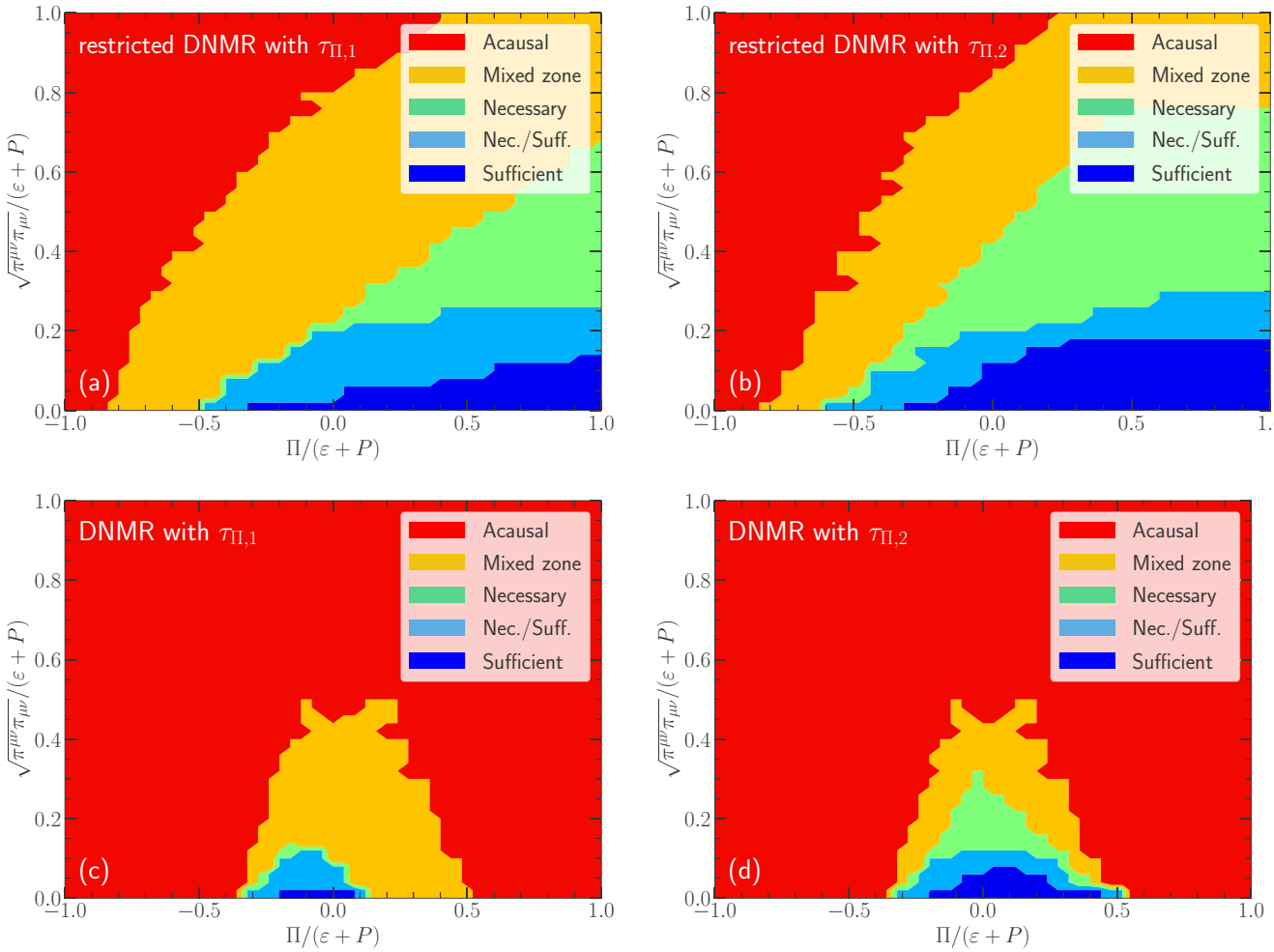

FIG. 3. Causal regions as functions of the inverse Reynolds numbers for the shear and bulk viscosity. The restricted and full DNMR hydrodynamic theories with two different forms of the bulk relaxation time are presented.

From the similarity transformation, the inverse Reynolds number R_π is related to the eigenvalues of the shear stress tensor by

$$R_\pi = \sqrt{\left(\frac{\Lambda_1}{\varepsilon+P}\right)^2 + \left(\frac{\Lambda_2}{\varepsilon+P}\right)^2 + \left(\frac{\Lambda_3}{\varepsilon+P}\right)^2}. \tag{16}$$

Using the tracelessness condition for the shear stress tensor, we can derive the following inequality,

$$\frac{\sqrt{6}}{2}\frac{\Lambda_{\max}}{\varepsilon+P} \leqslant R_\pi \leqslant \sqrt{2}\frac{\Lambda_{\max}}{\varepsilon+P}, \tag{17}$$

where $\Lambda_{\max} \equiv \max\{|\Lambda_1|, |\Lambda_2|, |\Lambda_3|\}$ is the maximum absolute eigenvalue of $\pi^{\mu\nu}$.

III. RESULTS

A. Visualizing the causal regions with inverse Reynolds numbers

Before examining the causality conditions in event-by-event hydrodynamic simulations, we first identify the causal region in terms of the inverse Reynolds numbers.

Figure 3 demonstrates the causal regions with different choices of second-order transport coefficients listed in Table I. We test both the necessary and sufficient causality conditions in a five-dimensional space of $\{c_s^2, \Lambda_1, \Lambda_2, \Lambda_3, \Pi\}$, where c_s^2 varies between 0.15 to 1/3 and $\{\Lambda_i\}$ and Π varies from 0 to $\varepsilon + P$. Here, we present the causal regions in terms of the shear and bulk inverse Reynolds numbers. These two variables represent how far a fluid cell is out of equilibrium at a given space-time position. The red regions in the Fig. 3 violate the necessary causality conditions. Fluid cells in this region violate causality for sure. The yellow bands indicate a mixed region, where some fluid cells satisfy the necessary causality conditions and some are acausal, depending on exact values of c_s^2 and the shear $\{\Lambda_i\}$. Fluid cells with R_π and R_Π in the green areas satisfy the necessary causality conditions but violate the sufficient conditions. The light blue region contains a mixture of fluid cells that satisfy or violate the sufficient conditions. The current causality conditions are not sufficient to determine whether fluid cells are causal or not in yellow, green, and light blue regions. Finally, the dark blue regions show the inverse Reynolds numbers allowed by the sufficient causality conditions in which fluid cells are causal.

The causality conditions impose maximum allowed values for the inverse Reynolds numbers R_π and $|R_\Pi|$ during the hydrodynamic evolution. Because the bulk viscous pressure acts

against the local expansion rate $\theta = \partial_\mu u^\mu$, its value relaxes to the negative Navier-Stokes value $\Pi \sim -\zeta\theta$, and so R_Π is negative in most cases. Figure 3 show that the necessary causality conditions require $R_\pi < 1$ and $|R_\Pi| < 1$ when $R_\Pi < 0$ for the DNMR hydrodynamics. The sufficient conditions require extremely small viscous corrections, $R_\pi \leqslant 0.1$, when the bulk viscous pressure is negative.

Comparing Figs. 3(a) and 3(b), we find that the bulk relaxation time $\tau_{\Pi,2}$ allows a larger causal region than that with $\tau_{\Pi,1}$, which is consistent with the static conditions n_{static} shown in Fig. 1. The mixed zone is large for $\tau_{\Pi,1}$ because of its fast quadratic dependence on c_s^2. For Israel-Stewart theory, the causal region becomes bigger when $R_\Pi > 0$, when the terms with R_Π give opposite contributions in Eqs. (7)–(12) compared to those with the shear stress tensor.

Comparing Figs. 3(a) [3(b)] with Figs. 3(c) [3(d)], we find the allowed causal region shrinks significantly, especially for $R_\Pi > 0$ for the full DNMR theory. Because the sign for $(1 - \frac{2}{3}\frac{\lambda_{\pi\Pi}}{\tau_\pi} - \frac{\delta_{\Pi\Pi}}{\tau_\Pi} - c_s^2)$ in Eq. (12) flips from positive to negative with $\lambda_{\pi\Pi}/\tau_\pi = 6/5$, regions with large positive R_Π values are not allowed anymore. Figures 3(a) [3(b)] versus 3(c) [3(d)] visually show that the nonzero second-order transport coefficients $\{\tau_{\pi\pi}, \lambda_{\pi\Pi}, \lambda_{\Pi\pi}\}$ set strong restrictions on the size of shear stress tensor $\pi^{\mu\nu}$ and bulk viscous pressure Π. With these additional second-order transport coefficients, the inverse Reynolds numbers need to be smaller than 0.5 for both choices of bulk relaxation time.

In practice, numerical simulations were found to be stable when $R_\pi \leqslant 1$ and $|R_\Pi| \leqslant 1$ with a grid spacing $dx = 0.067$ fm [35]. These stability conditions are less demanding compared to the causal regions shown in Fig. 3.

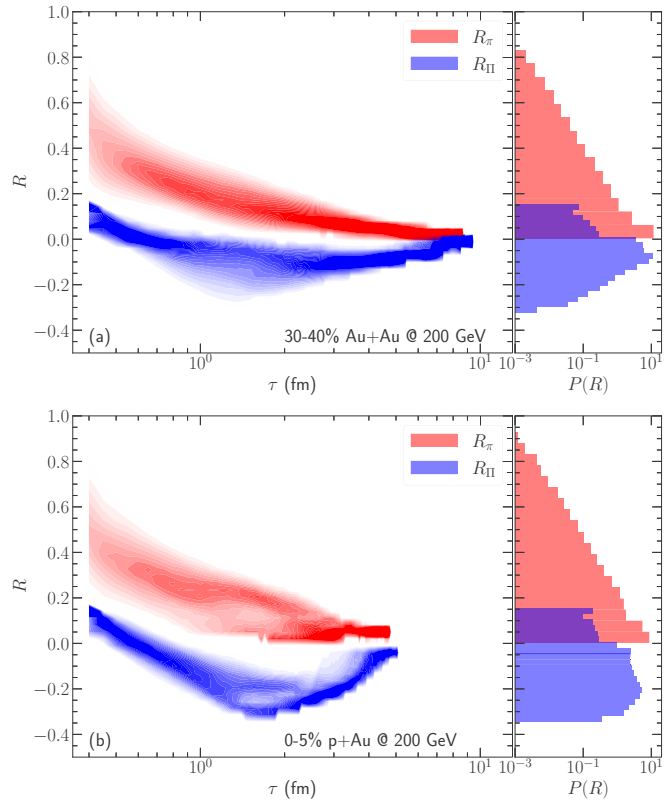

FIG. 4. The distributions of fluid cells' inverse Reynolds numbers as a function of the longitudinal proper time for one 30–40% Au+Au collision (a) and one 0–5% p+Au collision (b) at the top RHIC energy. The right panels show the time-integrated probability distributions of the inverse Reynolds numbers.

B. Examining realistic hydrodynamic simulations

After identifying the causal regions in terms of inverse Reynolds number, we would like to find the limits on R_π and R_Π to ensure all fluid cells in hydrodynamic simulations are within the causal region. Those limits would be handy when performing large-scale event-by-event simulations.

It is instructive to first study the inverse Reynolds numbers' distributions as functions of the evolution time in relativistic hydrodynamic simulations. We analyze typical hydrodynamic evolution for 30–40% Au+Au and 0–5% p+Au collisions at the top RHIC energy using the IP-Glasma + MUSIC + UrQMD framework [35]. In this hybrid framework, the system's initial energy-momentum tensor is generated by the impact parameter dependent Glasma initial condition model (IP-Glasma). It is coupled with hydrodynamic simulations solved by the MUScl for Ion Collisions (MUSIC) code package, which is based on the MUScl-type (Monotonic Upstream-centered Schemes for Conservation Laws) finite volume method. As the system evolves to dilute densities, fluid cells are converted to particles and further propagate in a hadronic transport model, Ultra relativistic Quantum Molecular Dynamics (UrQMD). Figure 4 shows the time-dependent and time-integrated distributions of R_π and R_Π for fluid cells with temperature $T \geqslant 145$ MeV.

The maximum of the shear inverse Reynolds number reaches around one at the starting time of hydrodynamics $\tau_0 = 0.4\,\text{fm}/c$. Most of the fluid cells have an average $R_\pi \approx 0.3$ during the first fm/c of the hydrodynamic evolution in 30–40% Au+Au and 0–5% p+Au collisions. The bulk inverse Reynolds numbers start with positive values (0.05–0.15) at $\tau_0 = 0.4\,\text{fm}/c$ to compensate for the difference between the trace anomaly in lattice QCD EoS and the traceless energy stress tensor from the IP-Glasma phase [35,54]. As the bulk viscous pressure evolves towards its Navier-Stokes limit $-\zeta\theta$, most of the fluid cells' R_Π evolve to negative values during the first 0.5 fm/c and reach their minima around $\tau = 1.5$–$2\,\text{fm}/c$. Since the more compact 0–5% p+Au collision develops a larger expansion rate than that in 30–40% Au+Au collisions, the R_Π distribution has a peak around -0.2 in central p+Au collisions while most of the fluid cells have $|R_\Pi| < 0.1$ in 30–40% Au+Au collisions. For $\tau > 2\,\text{fm}/c$, the absolute values of R_π and R_Π decrease with τ because the local velocity gradients decrease with the evolution time.

Figure 5 shows the probability distribution of each causality measure in Eqs. (7) to (12) in realistic hydrodynamic simulations [35]. We find that there are 3.8% of the fluid cells in 30–40% Au+Au collisions violate the necessary causality conditions. The fraction of violating fluid cells increases to 17% in 0–5% p+Au collisions. The strong pressure gradients in the p+Au collision lead to fast expansion and drive the system out of equilibrium. Hence, simulating small systems

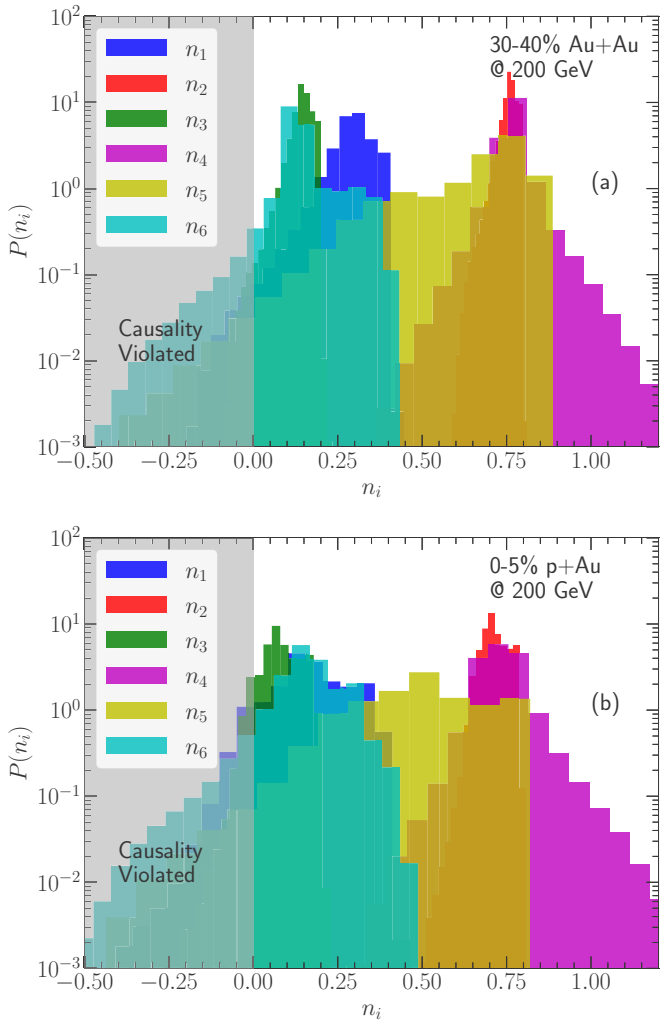

FIG. 5. Probability distributions for the necessary causality measures in fluid cells with temperature above 145 MeV in a typical Au+Au collision at 30–40% centrality (a) and a 0–5% p+Au collision (b) at 200 GeV. Hydrodynamic evolution is simulated with the DNMR equation of motion and the bulk relaxation time $\tau_{\Pi,1}$. During the evolution, we restrict $R_\pi \leqslant 1$ and $|R_\Pi| \leqslant 1$.

is more challenging than large collision systems as they can evolve further away from local thermal equilibrium.

We find that the necessary causality conditions n_1, n_3, n_5, and n_6 effectively constrain the sizes of inverse Reynolds numbers in the DNMR hydrodynamics. Among them, the condition n_6 in Eq. (12) imposes the strongest constraint. Table II summarizes the fractions of fluid cells that violate necessary or sufficient causality conditions for different transport coefficient choices in hydrodynamic simulations. We note that there are significant fractions of fluid cells that satisfy the necessary conditions but violate the sufficient causality conditions. The current causality conditions cannot determine whether they violate causality. As shown in Fig. 3, we would need to impose very strong constraints $R_\pi \ll 1$ and $|R_\Pi| \ll 1$ to ensure all fluid cells to satisfy the sufficient conditions, which significantly limits simulating viscous effects in relativistic hydrodynamic evolution. We note that Fig. 5 and Table II here summarize the overall fraction of fluid cells violate the necessary and sufficient causality conditions. Because the inverse Reynolds numbers are large during the early time of the evolution as shown in Fig. 4, the violation of causality could potentially play a substantial role during the first few fm/c of the hydrodynamic evolution. A quantitative time differential analysis was presented in a recent work [55].

To regulate all fluid cells that violate the necessary causality conditions, we need to impose restrictions on inverse Reynolds number sizes during hydrodynamic evolution. In Fig. 6, we find that imposing $R_\pi \leqslant \sqrt{2}P/(\varepsilon + P)$ and $|R_\Pi| \leqslant P/(\varepsilon + P)$ can ensure all the fluid cells in the 30–40% Au+Au and 0–5% p+Au collisions at 200 GeV stay within the necessary causal region for the restricted DNMR hydrodynamics with $\tau_{\Pi,1}$. By setting the transport coefficients $\lambda_{\pi\Pi}$ and $\tau_{\pi\pi}$ to zero, the necessary condition measures n_1 and n_3 reduce to static inequalities that only depend on the C_η value. The condition n_6 imposes the dominant constraints. In Eq. (17), the inverse Reynolds number of the shear stress tenor $R_\pi \leqslant \sqrt{2}\Lambda_{\max}/(\varepsilon + P)$. If we choose $\Lambda_{\max} = P$, then $R_\pi \leqslant \sqrt{2}P/(\varepsilon + P)$. Condition $|R_\Pi| \leqslant P/(\varepsilon + P)$ is equivalent to $|\Pi|/P \leqslant 1$, making sure that the thermal pressure is larger than the bulk viscous pressure and the total pressure is positive. Therefore, this condition avoids the formation of unstable cavitation regions during the evolution [56–59].

We further examine the sufficient conditions after imposing the restrictions on the inverse Reynolds numbers and find the fractions of violating fluid cells remain almost unchanged as those in Table II. The detailed analysis is represented in the Appendix.

With the second choice of bulk relaxation time $\tau_{\Pi,2}$, the necessary causality conditions allow for larger values of the

TABLE II. The fractions of cells violate necessary or sufficient causality conditions in 30–40% Au+Au and 0–5% p+Au collisions at 200 GeV with different choices of transport coefficients. We restrict the inverse Reynolds numbers $R_\pi \leqslant 1$ and $|R_\Pi| \leqslant 1$.

Collision system	Transport coefficients	Violate necessary conditions	Violate sufficient conditions
30–40% Au+Au	Restricted DNMR with $\tau_{\Pi,1}$	1.8%	33%
	DNMR with $\tau_{\Pi,1}$	3.8%	22%
0–5% p+Au	Restricted DNMR with $\tau_{\Pi,1}$	9%	66%
	DNMR with $\tau_{\Pi,1}$	17%	48%
30–40% Au+Au	Restricted DNMR with $\tau_{\Pi,2}$	0.1%	14%
	DNMR with $\tau_{\Pi,2}$	1.7%	16%
0–5% p+Au	Restricted DNMR with $\tau_{\Pi,2}$	0.2%	25%
	DNMR with $\tau_{\Pi,2}$	7%	40%

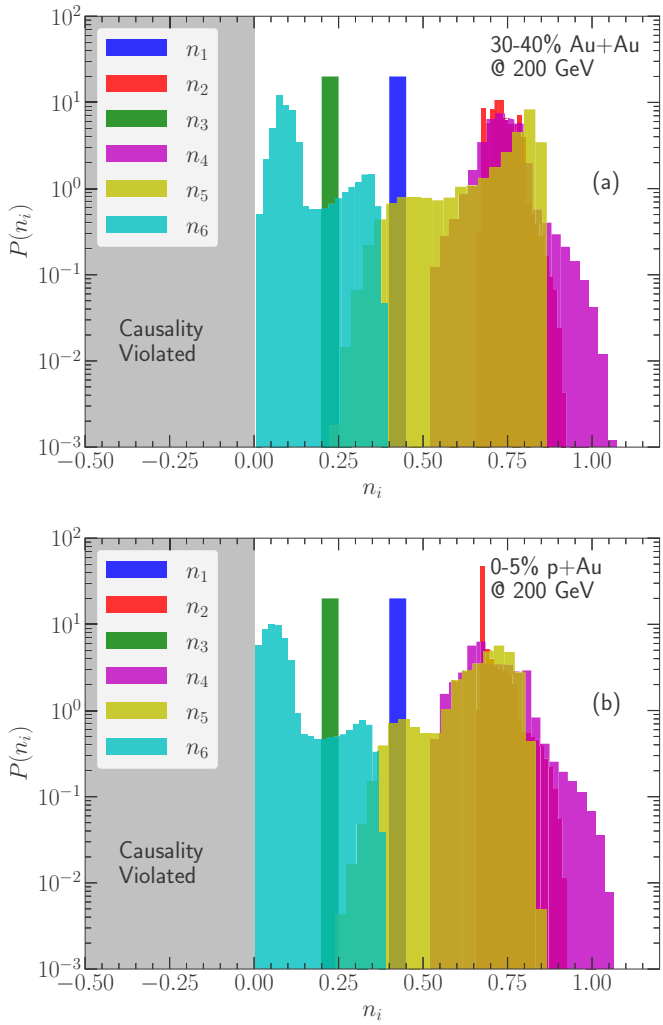

FIG. 6. Similar probability distributions as those in Fig. 5 but for hydrodynamic evolution simulated with the restricted DNMR equation of motion and the bulk relaxation time $\tau_{\Pi,1}$. During the evolution, we restrict $R_\pi \leqslant \sqrt{2}P/(\varepsilon + P)$ and $|R_\Pi| \leqslant P/(\varepsilon + P)$.

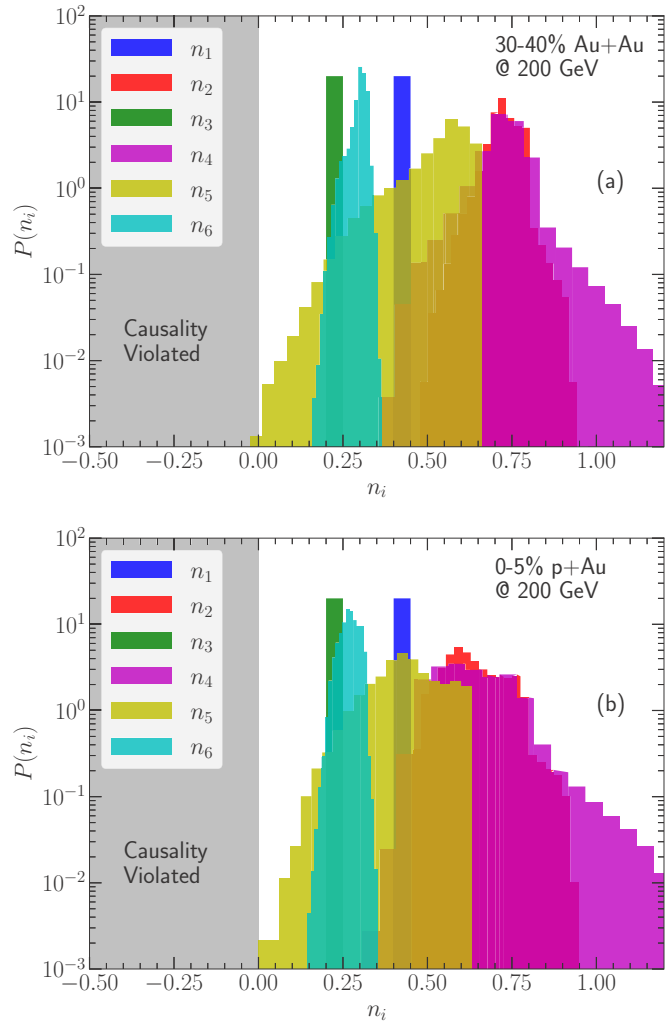

FIG. 7. Similar probability distributions as those in Fig. 5 but for hydrodynamic evolution simulated with the restricted DNMR equation of motion and the bulk relaxation time $\tau_{\Pi,2}$. During the evolution, we restrict $R_\pi \leqslant 0.6$ and $|R_\Pi| \leqslant 0.6$.

inverse Reynolds numbers during the hydrodynamic simulations than those with the $\tau_{\Pi,1}$. We find that requiring R_π and $|R_\Pi|$ to be smaller than 0.6 can ensure all the fluid cells within the causal region, shown in Fig. 7. Condition n_5 in Eq. (11) imposes the dominant constraints on the inverse Reynolds numbers in this case.

We find that with the bulk relaxation time $\tau_{\Pi,2}$, most of the fluid cells that violate the necessary causality conditions are at the first few time steps of the evolution, shown in Fig. 4. Because the early-stage heavy-ion collisions are far out of equilibrium, the necessary causality conditions set restrictions on when we can apply the relativistic viscous hydrodynamic description. Before applying the hydrodynamic framework to the system, we need to rely on effective kinetic theory to drive the system to be close enough to the local thermal equilibrium [60–63].

We note that choosing a slowly varying function for coefficient $C_\zeta(c_s^2)$ allows larger viscous corrections during the hydrodynamic evolution. In the simulations with the bulk relaxation time $\tau_{\Pi,1}$, a group of fluid cells near the transition region, where the square of sound speed is near 0.15, also violates the necessary causal conditions. Figure 1 shows that there is little room left for the dynamically evolving viscous tensor when $c_s^2 \approx 0.15$.

C. Effects of regulating viscous stress tensor with causality constraints on flow observables

Finally, we study the effects of imposing these restrictions on the inverse Reynolds numbers on flow observables.

Figure 8 shows the averaged transverse momentum $\langle p_T \rangle$ of pions compared with the PHENIX and STAR measurements in Au+Au collisions at the top RHIC energy [64,65] and the p_T-differential anisotropic flow coefficients $v_{2,3}\{2\}(p_T)$ in 30–40% centrality [66,67]. We first discuss the effects from the second-order transport coefficients $\{\tau_{\pi\pi}, \lambda_{\pi\Pi}, \lambda_{\Pi\pi}, \varphi_7\}$ on the flow observables. Comparing the black curves with red dashed lines, we find that these second-order terms in the

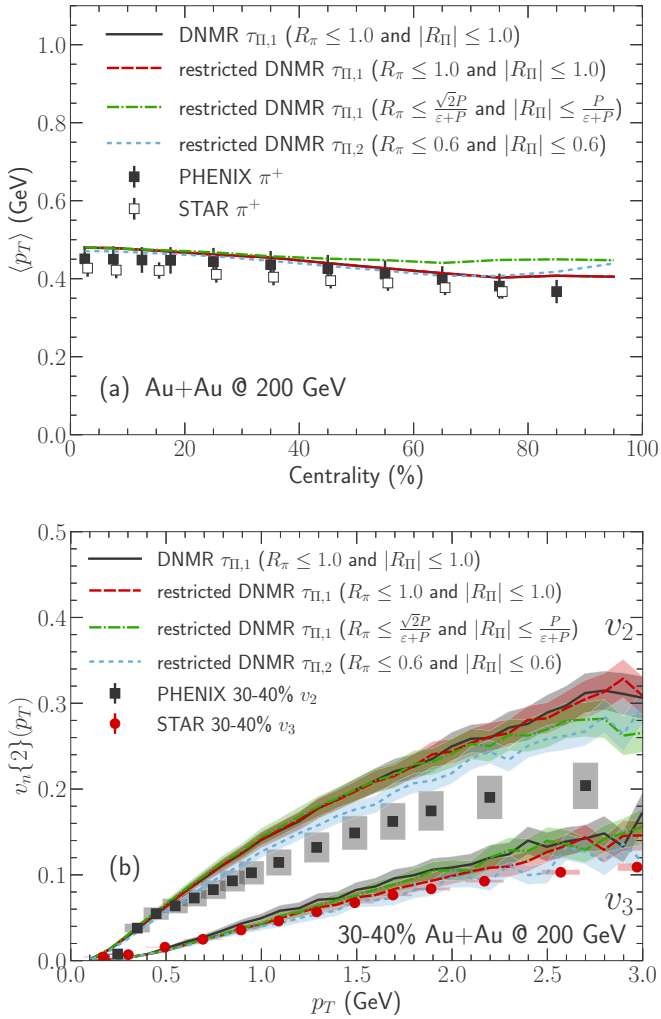

FIG. 8. The averaged transverse momentum $\langle p_T \rangle$ (a) and p_T-differential flow coefficients $v_n(p_T)$ (b) in Au+Au collisions at 200 GeV [64–67].

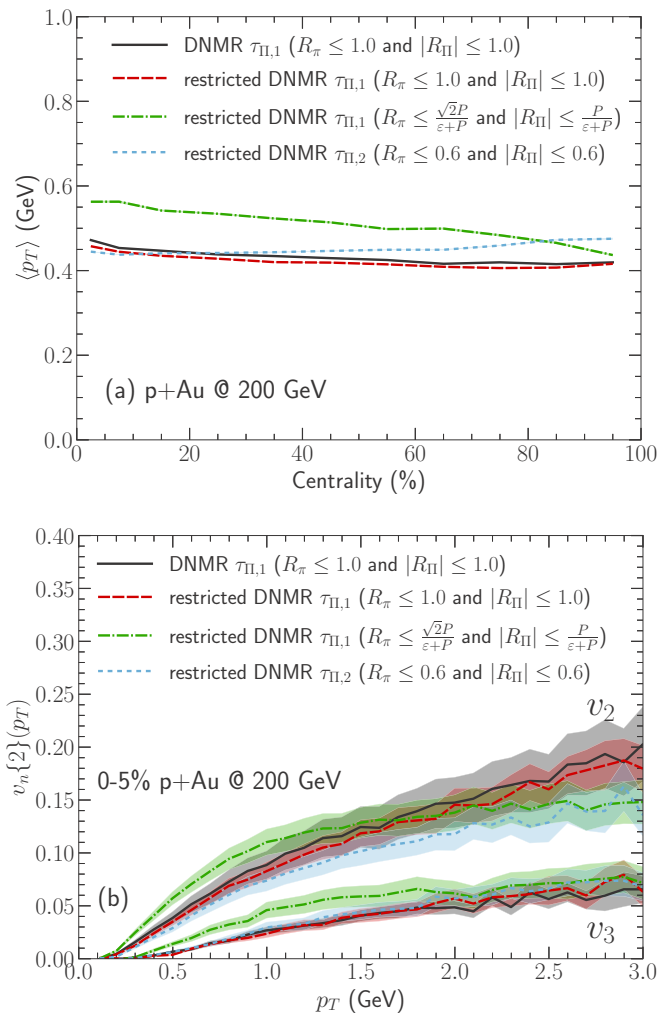

FIG. 9. The averaged transverse momentum $\langle p_T \rangle$ (a) and p_T-differential flow coefficients $v_n(p_T)$ (b) in p+Au collisions at 200 GeV.

hydrodynamic equations of motion have negligible effects on particle's averaged transverse momentum and p_T-differential anisotropic flow coefficients. Further imposing restrictions on the inverse Reynolds numbers, $R_\pi \leqslant \sqrt{2}P/(\varepsilon + P)$ and $|R_\Pi| \leqslant P/(\varepsilon + P)$, we ensure all the fluid cells satisfy the necessary causality conditions. We find negligible effects on the p_T-differential anisotropic flow coefficients. The pions' mean p_T increases by 5–10% in the peripheral centrality bins. With the second choice of the bulk relaxation time $\tau_{\Pi,2}$, the inverse Reynolds numbers are allowed to reach up to 0.6. Comparing the flow results from the two relaxation times, we see that the elliptic flow coefficient $v_2\{2\}(p_T)$ is ≈10% smaller with $\tau_{\Pi,2}$ than the results from simulations with $\tau_{\Pi,1}$ for $p_T \geqslant 1$ GeV. We checked that the additional second-order terms in the DNMR theory have less than 5% effects on observables in the simulations with bulk relaxation time $\tau_{\Pi,2}$.

Figure 9 shows the same flow observables for p+Au collisions at 200 GeV. Comparing the black and red curves, we find that the effects from the additional second-order transport coefficients in the DNMR theory remain negligible in the calculations. For p+Au collisions, restricting the inverse Reynolds numbers (green dash-dotted curves) leads to an ≈20% larger mean p_T for pions. We also find that these conditions result in 20–30% larger anisotropic flow coefficients $v_{2,3}$. These variations in observables are the direct consequence of restricting the viscous corrections in the simulations. The smaller shear and bulk viscous tensors allow for stronger anisotropic and radial flow during the hydrodynamic evolution, respectively. With the second choice of the bulk relaxation time, larger viscous corrections are allowed in the hydrodynamic evolution than those simulations with $\tau_{\Pi,1}$. With the necessary causality conditions fulfilled, the simulations with the relaxation time $\tau_{\Pi,2}$ have 20–30% smaller $v_{2,3}(p_T)$ for $p_T < 2$ GeV than those with $\tau_{\Pi,1}$.

IV. CONCLUSIONS

This work analyzes the full nonlinear necessary and sufficient causality conditions [28] in the relativistic hydrodynamic description of heavy-ion collisions. We visualize the causal regions as functions of the system's inverse Reynolds number for the restricted and full DNMR

hydrodynamic theories. We find the second-order transport coefficients $\{\tau_{\pi\pi}, \lambda_{\pi\Pi}, \lambda_{\Pi\pi}\}$ derived from kinetic theory with the 14-moment approximation set strong constraints on the maximum allowed inverse Reynolds numbers to satisfy causality. We explore simulations with two classes of bulk relaxation time derived from kinetic and strongly coupled theories.

We examine the causality conditions in the hydrodynamic evolution for a typical 30–40% Au+Au collision and a 0–5% p+Au collision at the top RHIC energy. We find that the conditions n_5 and n_6 in Eqs. (11) and (12) impose dominant constraints on the inverse Reynolds numbers' size. For restricted DNMR hydrodynamics with the bulk relaxation time $\tau_{\Pi,1}$ in Eq. (5), we find that $R_\pi \leqslant \sqrt{2}P/(\varepsilon + P)$ and $|R_\Pi| \leqslant P/(\varepsilon + P)$ can effectively ensure all fluid cells stay within the causal region. For simulations with the bulk relaxation time $\tau_{\Pi,2}$ in Eq. (6), the necessary causality conditions allow for inverse Reynolds numbers up to 0.6. Hence, larger shear and bulk viscosity can be used in hydrodynamic simulations with $\tau_{\Pi,2}$ than those in the simulations with $\tau_{\Pi,1}$.

We study how experimental flow observables are affected when imposing the necessary causality constraints on the inverse Reynolds numbers during hydrodynamic simulations. We find that the variations are within 10% for the pion's mean p_T- and p_T-differential anisotropic flow coefficients for Au+Au collisions at 200 GeV. Therefore, the previous results with $R_\pi \leqslant 1$ and $|R_\Pi| \leqslant 1$ remain reliable, although about 4% of the fluid cells violates causality. For the smaller p+Au collisions, sizable effects are present when we use the bulk relaxation time $\tau_{\Pi,1}$ in the simulations. Restricting the size of viscous stress tensor leads to 20% larger mean p_T and $v_{2,3}(p_T)$. The bulk relaxation time $\tau_{\Pi,2}$ allows for larger viscous corrections in numerical simulations, and the results are close to those in Ref. [35] while ensuring all fluid cells satisfy the necessary causality conditions.

Finally, we emphasize that numerical hydrodynamic codes should build in checks for causality conditions during the evolution. They are crucial for future large-scale Bayesian inference studies to extract the QGP transport coefficients from experimental measurements. On the one hand, the causality conditions limit the maximum allowed shear and bulk viscosity and their relaxation times in the prior of Bayesian calibration. On the other hand, our results suggest that regulating simulations with the necessary causality conditions could introduce a 20% theoretical uncertainty in Bayesian analysis with flow observables in peripheral AA and pA systems. Moreover, the causality conditions also limit when relativistic hydrodynamics can be applied at early time and request realistic pre-equilibrium dynamics. The free-streaming model used in previous Bayesian analysis [36–42] drives the collision system further away from local thermal equilibrium and increases shear stress tensor's size [68]. A long free-streaming time would drive fluid cells' inverse Reynolds number $\sqrt{\pi^{\mu\nu}\pi_{\mu\nu}}/P \to \sqrt{6}/2$ [68], which increases the violation of sufficient causality conditions and the theoretical uncertainty from regulating them at the beginning of the hydrodynamic phase. Therefore, it is essential to employ a realistic pre-equilibrium evolution based on effective kinetic theories, such as KøMPøST [60,61], to drive the collision system to the causal region before starting hydrodynamic simulations [55,62,63].

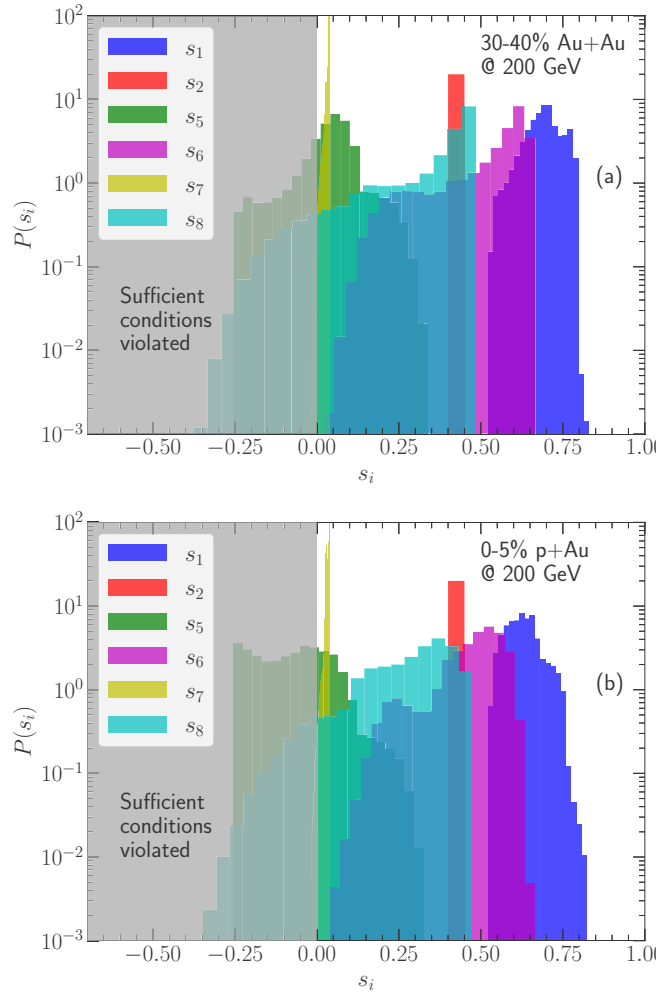

FIG. 10. Probability distributions for the sufficient causality measures in fluid cells with temperature above 145 MeV in a typical Au+Au collision at 30–40% centrality (a) and a 0–5% p+Au collision (b) at 200 GeV. Hydrodynamic evolution is simulated with the restricted DNMR equation of motion and the bulk relaxation time $\tau_{\Pi,1}$. During the evolution, we restrict $R_\pi \leqslant \sqrt{2}P/(\varepsilon + P)$ and $|R_\Pi| \leqslant P/(\varepsilon + P)$.

ACKNOWLEDGMENTS

We thank Charles Gale, Ulrich Heinz, Jorge Noronha, Jean-Francois Paquet, Bjoern Schenke, and Mayank Singh for fruitful discussion. This work is supported in part by the US Department of Energy (DOE) under Grant No. DE-SC0013460 and in part by the National Science Foundation (NSF) under Grant No. PHY-2012922. This research used resources of the National Energy Research Scientific Computing Center, which is supported by the Office of Science of the US Department of Energy under Contract No. DE-AC02-05CH11231, resources provided by the Open Science Grid, which is supported by the National Science Foundation and the US Department of Energy's Office of Science, and resources of the high-performance computing services at

Wayne State University. This work is supported in part by the US Department of Energy, Office of Science, Office of Nuclear Physics, within the framework of the Beam Energy Scan Theory (BEST) Topical Collaboration.

APPENDIX: SUFFICIENT CONDITIONS FOR CAUSALITY

Following Ref. [28], the sufficient conditions for causality can be rewritten as follows:

$$s_1 \equiv 1 - \frac{1}{C_\eta} - \frac{|\Lambda_1|}{\varepsilon + P} + \left(1 - \frac{\lambda_{\pi\Pi}}{2\tau_\pi}\right)\frac{\Pi}{\varepsilon + P} - \frac{\tau_{\pi\pi}}{2\tau_\pi}\frac{\Lambda_3}{\varepsilon + P} \geqslant 0, \tag{A1}$$

$$s_2 \equiv \frac{1}{C_\eta} + \frac{\lambda_{\pi\Pi}}{2\tau_\pi}\frac{\Pi}{\varepsilon + P} - \frac{\tau_{\pi\pi}}{2\tau_\pi}\frac{|\Lambda_1|}{\varepsilon + P} \geqslant 0, \tag{A2}$$

$$s_3 \equiv 6\frac{\delta_{\pi\pi}}{\tau_\pi} - \frac{\tau_{\pi\pi}}{\tau_\pi} \geqslant 0, \tag{A3}$$

$$s_4 \equiv \frac{\lambda_{\Pi\pi}}{\tau_\Pi} + c_s^2 - \frac{\tau_{\pi\pi}}{12\tau_\pi} \geqslant 0, \tag{A4}$$

$$s_5 \equiv \left(1 + \frac{\Pi}{\varepsilon + P}\right)(1 - c_s^2) - \left[\frac{4}{3}\frac{1}{C_\eta} + \frac{1}{C_\zeta} + \left(\frac{2}{3}\frac{\lambda_{\pi\Pi}}{\tau_\pi} + \frac{\delta_{\Pi\Pi}}{\tau_\Pi}\right)\frac{\Pi}{\varepsilon + P} + \left(\frac{\delta_{\pi\pi}}{\tau_\pi} + \frac{\tau_{\pi\pi}}{3\tau_\pi} + \frac{\lambda_{\Pi\pi}}{\tau_\Pi} + c_s^2\right)\frac{\Lambda_3}{\varepsilon + P} + \frac{|\Lambda_1|}{\varepsilon + P} + \frac{\left(\frac{\delta_{\pi\pi}}{\tau_\pi} - \frac{\tau_{\pi\pi}}{12\tau_\pi}\right)\left(\frac{\lambda_{\Pi\pi}}{\tau_\Pi} + c_s^2 - \frac{\tau_{\pi\pi}}{12\tau_\pi}\right)\left(\frac{\Lambda_3}{\varepsilon+P} + \frac{|\Lambda_1|}{\varepsilon+P}\right)^2}{1 - \frac{1}{C_\eta} + \left(1 - \frac{\lambda_{\pi\Pi}}{2\tau_\pi}\right)\frac{\Pi}{\varepsilon+P} - \frac{|\Lambda_1|}{\varepsilon+P} - \frac{\tau_{\pi\pi}}{2\tau_\pi}\frac{\Lambda_3}{\varepsilon+P}}\right] \geqslant 0, \tag{A5}$$

$$s_6 \equiv \frac{1}{3C_\eta} + \frac{1}{C_\zeta} + c_s^2 + \left(\frac{\lambda_{\pi\Pi}}{6\tau_\pi} + \frac{\delta_{\Pi\Pi}}{\tau_\Pi} + c_s^2\right)\frac{\Pi}{\varepsilon + P} + \left(\frac{\tau_{\pi\pi}}{6\tau_\pi} - \frac{\delta_{\pi\pi}}{\tau_\pi} + \frac{\lambda_{\Pi\pi}}{\tau_\Pi} - c_s^2\right)\frac{|\Lambda_1|}{\varepsilon + P} \geqslant 0, \tag{A6}$$

$$s_7 \equiv \left[\frac{1}{C_\eta} + \frac{\lambda_{\pi\Pi}}{2\tau_\pi}\frac{\Pi}{\varepsilon + P} - \frac{\tau_{\pi\pi}}{2\tau_\pi}\frac{|\Lambda_1|}{\varepsilon + P}\right]^2 - \left(\frac{\delta_{\pi\pi}}{\tau_\pi} - \frac{\tau_{\pi\pi}}{12\tau_\pi}\right)\left(\frac{\lambda_{\Pi\pi}}{\tau_\Pi} + c_s^2 - \frac{\tau_{\pi\pi}}{12\tau_\pi}\right)\left(\frac{\Lambda_3}{\varepsilon + P} + \frac{|\Lambda_1|}{\varepsilon + P}\right)^2 \geqslant 0, \tag{A7}$$

$$s_8 \equiv \frac{4}{3C_\eta} + \frac{1}{C_\zeta} + c_s^2 + \left(\frac{2}{3}\frac{\lambda_{\pi\Pi}}{\tau_\pi} + \frac{\delta_{\Pi\Pi}}{\tau_\Pi} + c_s^2\right)\frac{\Pi}{\varepsilon + P} - \left(\frac{\delta_{\pi\pi}}{\tau_\pi} + \frac{\tau_{\pi\pi}}{3\tau_\pi} - \frac{\lambda_{\Pi\pi}}{\tau_\Pi} + c_s^2\right)\frac{|\Lambda_1|}{\varepsilon + P} - \frac{\left(1 + \frac{\Pi}{\varepsilon+P} + \frac{\Lambda_2}{\varepsilon+P}\right)\left(1 + \frac{\Pi}{\varepsilon+P} + \frac{\Lambda_3}{\varepsilon+P}\right)}{3\left(1 + \frac{\Pi}{\varepsilon+P} - \frac{|\Lambda_1|}{\varepsilon+P}\right)^2} \times \left[1 + \frac{2}{C_\eta} + \left(1 + \frac{\lambda_{\pi\Pi}}{\tau_\pi}\right)\frac{\Pi}{\varepsilon + P} - \frac{|\Lambda_1|}{\varepsilon + P} + \frac{\tau_{\pi\pi}}{\tau_\pi}\frac{\Lambda_3}{\varepsilon + P}\right] \geqslant 0. \tag{A8}$$

Because the conditions s_3 and s_4 do not depend on the dynamical evolution shear stress tensor and bulk viscous pressure, we do not need to check them during the hydrodynamic evolution.

In Fig. 10, we show the probability distributions of sufficient causality conditions' measures for 30–40% Au+Au and 0–5% p+Au collisions at 200 GeV. Most of the violating fluid cells fail the conditions s_5 and s_8 in Eqs. (A5) and (A8). Here, we already restrict the inverse Reynolds number $R_\pi \leqslant \sqrt{2}P/(\varepsilon + P)$ and $|R_\Pi| \leqslant P/(\varepsilon + P)$ to ensure all the fluid cells fulfill the necessary causality conditions. However, these restrictions on R_π and R_Π do not reduce the fractions of fluid cells that violate the sufficient conditions.

[1] P. Romatschke, New developments in relativistic viscous hydrodynamics, Int. J. Mod. Phys. E **19**, 1 (2010).

[2] U. Heinz and R. Snellings, Collective flow and viscosity in relativistic heavy-ion collisions, Ann. Rev. Nucl. Part. Sci. **63**, 123 (2013).

[3] C. Gale, S. Jeon, and B. Schenke, Hydrodynamic modeling of heavy-ion collisions, Int. J. Mod. Phys. A **28**, 1340011 (2013).

[4] Li Yan, A flow paradigm in heavy-ion collisions, Chin. Phys. C **42**, 042001 (2018).

[5] W. Florkowski, M. P. Heller, and M. Spalinski, New theories of relativistic hydrodynamics in the LHC era, Rept. Prog. Phys. **81**, 046001 (2018).

[6] P. Romatschke and U. Romatschke, *Relativistic Fluid Dynamics In and Out of Equilibrium*, Cambridge Monographs on Mathematical Physics (Cambridge University Press, Cambridge, UK, 2019).

[7] C. Shen and Li Yan, Recent development of hydrodynamic modeling in heavy-ion collisions, Nucl. Sci. Tech. **31**, 122 (2020).

[8] P. Romatschke and U. Romatschke, Viscosity Information from Relativistic Nuclear Collisions: How Perfect is the Fluid Observed at RHIC? Phys. Rev. Lett. **99**, 172301 (2007).

[9] H. Song, S. A. Bass, U. Heinz, T. Hirano, and C. Shen, 200 *A* GeV Au+Au Collisions Serve a Nearly Perfect Quark-Gluon Liquid, Phys. Rev. Lett. **106**, 192301 (2011); **109**, 139904(E) (2012).

[10] C. Shen and U. Heinz, Hydrodynamic flow in heavy-ion collisions with large hadronic viscosity, Phys. Rev. C **83**, 044909 (2011).

[11] C. Gale, S. Jeon, B. Schenke, P. Tribedy, and R. Venugopalan, Event-By-Event Anisotropic Flow in Heavy-Ion Collisions from Combined Yang-Mills and Viscous Fluid Dynamics, Phys. Rev. Lett. **110**, 012302 (2013).

[12] S. Ryu, J. F. Paquet, C. Shen, G. S. Denicol, B. Schenke, S. Jeon, and C. Gale, Importance of the Bulk Viscosity of QCD in Ultrarelativistic Heavy-Ion Collisions, Phys. Rev. Lett. **115**, 132301 (2015).

[13] C. Shen and U. Heinz, The road to precision: Extraction of the specific shear viscosity of the quark-gluon plasma, Nucl. Phys. News **25**, 6 (2015).

[14] A. Majumder and C. Shen, Suppression of the High p_T Charged Hadron R_{AA} at the LHC, Phys. Rev. Lett. **109**, 202301 (2012).

[15] K. M. Burke, A. Buzzatti, N. Chang, C. Gale, M. Gyulassy, U. Heinz, S. Jeon, A. Majumder, B. Muller, G. Qin *et al.* (JET Collaboration), Extracting the jet transport coefficient from jet quenching in high-energy heavy-ion collisions, Phys. Rev. C. **90**, 014909 (2014).

[16] C. Shen, Recent developments in the theory of electromagnetic probes in relativistic heavy-ion collisions, Nucl. Part. Phys. Proc. **276-278**, 77 (2016).

[17] C. Shen, Electromagnetic radiation from QCD matter: Theory overview, Nucl. Phys. A **956**, 184 (2016).

[18] J.-F. Paquet, C. Shen, G. S. Denicol, M. Luzum, B. Schenke, S. Jeon, and C. Gale, Production of photons in relativistic heavy-ion collisions, Phys. Rev. C **93**, 044906 (2016).

[19] G. Vujanovic, J.-F. Paquet, C. Shen, G. S. Denicol, S. Jeon, C. Gale, and U. Heinz, Exploring the influence of bulk viscosity of QCD on dilepton tomography, Phys. Rev. C **101**, 044904 (2020).

[20] A. Kumar, A. Majumder, and C. Shen, Energy and scale dependence of $\hat{q}$ and the JET puzzle, Phys. Rev. C **101**, 034908 (2020).

[21] Y. Tachibana, C. Shen, and A. Majumder, Bulk medium evolution has considerable effects on jet observables!, arXiv:2001.08321.

[22] W. A. Hiscock and L. Lindblom, Stability and causality in dissipative relativistic fluids, Ann. Phys. **151**, 466 (1983).

[23] T. S. Olson, Stability and causality in the Istrael-Stewart energy frame theory, Ann. Phys. **199**, 18 (1990).

[24] S. Pu, T. Koide, and D. H. Rischke, Does stability of relativistic dissipative fluid dynamics imply causality? Phys. Rev. D **81**, 114039 (2010).

[25] X.-G. Huang, T. Kodama, T. Koide, and D. H. Rischke, Bulk viscosity and relaxation time of causal dissipative relativistic fluid dynamics, Phys. Rev. C **83**, 024906 (2011).

[26] G. S. Denicol, T. Kodama, T. Koide, and P. Mota, Stability and Causality in relativistic dissipative hydrodynamics, J. Phys. G **35**, 115102 (2008).

[27] S. Floerchinger and E. Grossi, Causality of fluid dynamics for high-energy nuclear collisions, J. High Energy Phys. 08 (2018) 186.

[28] F. S. Bemfica, M. M. Disconzi, V. Hoang, J. Noronha, and M. Radosz, Nonlinear constraints on relativistic fluids far from equilibrium, arXiv:2005.11632.

[29] W. Israel, Nonstationary irreversible thermodynamics: A causal relativistic theory, Ann. Phys. **100**, 310 (1976).

[30] W. Israel and J. M. Stewart, Transient relativistic thermodynamics and kinetic theory, Ann. Phys. **118**, 341 (1979).

[31] I. Muller, Zum Paradoxon der Warmeleitungstheorie, Z. Phys. **198**, 329 (1967).

[32] G. S. Denicol, H. Niemi, E. Molnar, and D. H. Rischke, Derivation of transient relativistic fluid dynamics from the Boltzmann equation, Phys. Rev. D **85**, 114047 (2012); **91**, 039902(E) (2015).

[33] C. Shen, Z. Qiu, H. Song, J. Bernhard, S. Bass, and U. Heinz, The iEBE-VISHNU code package for relativistic heavy-ion collisions, Comput. Phys. Commun. **199**, 61 (2016).

[34] G. S. Denicol, C. Gale, S. Jeon, A. Monnai, B. Schenke, and C. Shen, Net baryon diffusion in fluid dynamic simulations of relativistic heavy-ion collisions, Phys. Rev. C **98**, 034916 (2018).

[35] B. Schenke, C. Shen, and P. Tribedy, Running the gamut of high energy nuclear collisions, Phys. Rev. C **102**, 044905 (2020).

[36] J. E. Bernhard, J. S. Moreland, S. A. Bass, J. Liu, and U. Heinz, Applying Bayesian parameter estimation to relativistic heavy-ion collisions: Simultaneous characterization of the initial state and quark-gluon plasma medium, Phys. Rev. C **94**, 024907 (2016).

[37] J. S. Moreland, J. E. Bernhard, and S. A. Bass, Bayesian calibration of a hybrid nuclear collision model using *p*-Pb and Pb-Pb data at energies available at the CERN Large Hadron Collider, Phys. Rev. C **101**, 024911 (2020).

[38] J. E. Bernhard, J. S. Moreland, and S. A. Bass, Bayesian estimation of the specific shear and bulk viscosity of quark–gluon plasma, Nat. Phys. **15**, 1113 (2019).

[39] D. Everett, W. Ke, J.-F. Paquet, G. Vujanovic, S. A. Bass, L. Du, C. Gale, M. Heffernan, U. Heinz, D. Liyanage *et al.* (JETSCAPE Collaboration), Phenomenological constraints on the transport properties of QCD matter with datadriven model averaging, arXiv:2010.03928.

[40] D. Everett, W. Ke, J.-F. Paquet, G. Vujanovic, S. A. Bass, L. Du, C. Gale, M. Heffernan, U. Heinz, D. Liyanage *et al.* (JETSCAPE Collaboration), Multisystem Bayesian constraints on the transport coefficients of QCD matter, Phys. Rev. C **103**, 054904 (2021).

[41] G. Nijs, W. Van Der Schee, U. Gürsoy, and R. Snellings, A Bayesian analysis of heavy ion collisions with trajectum, Phys. Rev. C **103**, 054909 (2021).

[42] G. Nijs, W. van der Schee, U. Gürsoy, and R. Snellings, A transverse momentum differential global analysis of heavy ion collisions, Phys. Rev. Lett. **126**, 202301 (2021).

[43] M. A. York and G. D. Moore, Second order hydrodynamic coefficients from kinetic theory, Phys. Rev. D **79**, 054011 (2009).

[44] J. Ghiglieri, G. D. Moore, and D. Teaney, Second-Order Hydrodynamics in Next-To-Leading-Order QCD, Phys. Rev. Lett. **121**, 052302 (2018).

[45] R. Baier, P. Romatschke, D. T. Son, A. O. Starinets, and M. A. Stephanov, Relativistic viscous hydrodynamics, conformal invariance, and holography, J. High Energy Phys. 04 (2008) 100.

[46] S. I. Finazzo, R. Rougemont, H. Marrochio, and J. Noronha, Hydrodynamic transport coefficients for the non-conformal quark-gluon plasma from holography, J. High Energy Phys. 02 (2015) 051.

[47] S. S. Gubser, A. Nellore, S. S. Pufu, and F. D. Rocha, Thermodynamics and Bulk Viscosity of Approximate Black Hole Duals to Finite Temperature Quantum Chromodynamics, Phys. Rev. Lett. **101**, 131601 (2008).

[48] I. Kanitscheider and K. Skenderis, Universal hydrodynamics of non-conformal branes, J. High Energy Phys. 04 (2009) 062.

[49] R. Rougemont, R. Critelli, J. Noronha-Hostler, J. Noronha, and C. Ratti, Dynamical versus equilibrium properties of the QCD phase transition: A holographic perspective, Phys. Rev. D **96**, 014032 (2017).

[50] G. S. Denicol, S. Jeon, and C. Gale, Transport coefficients of bulk viscous pressure in the 14-moment approximation, Phys. Rev. C **90**, 024912 (2014).

[51] N. Summerfield, B.-N. Lu, C. Plumberg, D. Lee, J. Noronha-Hostler, and A. Timmins, ^{16}O ^{16}O at RHIC and the LHC comparing α clustering vs substructure, arXiv:2103.03345.

[52] A. Bazavov, Tanmoy Bhattacharya, C. DeTar, H.-T. Ding, Steven Gottlieb, Rajan Gupta, P. Hegde, U. M. Heller, F. Karsch, E. Laermann *et al.* (HotQCD Collaboration), Equation of state in (2+1)-flavor QCD, Phys. Rev. D **90**, 094503 (2014).

[53] J. S. Moreland and R. A. Soltz, Hydrodynamic simulations of relativistic heavy-ion collisions with different lattice quantum chromodynamics calculations of the equation of state, Phys. Rev. C **93**, 044913 (2016).

[54] H. Mäntysaari, B. Schenke, C. Shen, and P. Tribedy, Imprints of fluctuating proton shapes on flow in proton-lead collisions at the LHC, Phys. Lett. B **772**, 681 (2017).

[55] C. Plumberg, D. Almaalol, T. Dore, J. Noronha, and J. Noronha-Hostler, Causality violations in realistic simulations of heavy-ion collisions, arXiv:2103.15889.

[56] G. Torrieri and I. Mishustin, Instability of Boost-invariant hydrodynamics with a QCD inspired bulk viscosity, Phys. Rev. C **78**, 021901(R) (2008).

[57] K. Rajagopal and N. Tripuraneni, Bulk viscosity and cavitation in boost-invariant hydrodynamic expansion, J. High Energy Phys. 03 (2010) 018.

[58] G. S. Denicol, C. Gale, and S. Jeon, The domain of validity of fluid dynamics and the onset of cavitation in ultrarelativistic heavy ion collisions, PoS **217**, 033 (2015).

[59] M. Byres, S. H. Lim, C. McGinn, J. Ouellette, and J. L. Nagle, Bulk viscosity and cavitation in heavy ion collisions, Phys. Rev. C **101**, 044902 (2020).

[60] A. Kurkela, A. Mazeliauskas, J.-F. Paquet, S. Schlichting, and D. Teaney, Matching the Nonequilibrium Initial Stage of Heavy Ion Collisions to Hydrodynamics with QCD Kinetic Theory, Phys. Rev. Lett. **122**, 122302 (2019).

[61] A. Kurkela, A. Mazeliauskas, J.-F. Paquet, S. Schlichting, and D. Teaney, Effective kinetic description of event-by-event pre-equilibrium dynamics in high-energy heavy-ion collisions, Phys. Rev. C **99**, 034910 (2019).

[62] C. Gale, J.-F. Paquet, B. Schenke, and C. Shen, Probing early-time dynamics and quark-gluon plasma transport properties with photons and hadrons, Nucl. Phys. A **1005**, 121863 (2021).

[63] T. Nunes da Silva, D. Chinellato, M. Hippert, W. Serenone, J. Takahashi, G. S. Denicol, M. Luzum, and J. Noronha, Pre-hydrodynamic evolution and its signatures in final-state heavy-ion observables, Phys. Rev. C **103**, 054906 (2021).

[64] S.S. Adler, S. Afanasiev, C. Aidala, N.N. Ajitanand, Y. Akiba, J. Alexander, R. Amirikas, L. Aphecetche, S.H. Aronson, R. Averbeck *et al.* (PHENIX Collaboration), Identified charged particle spectra and yields in Au+Au collisions at $\sqrt{S_{NN}} = 200$ GeV, Phys. Rev. C **69**, 034909 (2004).

[65] B. I. Abelev, M. M. Aggarwal, Z. Ahammed, B. D. Anderson, D. Arkhipkin, G. S. Averichev, Y. Bai, J. Balewski, O. Barannikova, L. S. Barnby *et al.* (STAR Collaboration), Systematic measurements of identified particle spectra in pp, d+Au and Au+Au collisions from STAR, Phys. Rev. C **79**, 034909 (2009).

[66] A. Adare, S. Afanasiev, C. Aidala, N.N. Ajitanand, Y. Akiba, H. Al-Bataineh, J. Alexander, K. Aoki, Y. Aramaki, E.T. Atomssa *et al.* (PHENIX Collaboration), Measurements of Higher-Order Flow Harmonics in Au+Au Collisions at $\sqrt{s_{NN}} = 200$ GeV, Phys. Rev. Lett. **107**, 252301 (2011).

[67]] L. Adamczyk, J. K. Adkins, G. Agakishiev, M. M. Aggarwal, Z. Ahammed, A. V. Alakhverdyants, I. Alekseev, J. Alford, C. D. Anson, D. Arkhipkin *et al.* (STAR Collaboration), Third harmonic flow of charged particles in Au+Au collisions at $\sqrt{S_{NN}} = 200$ GeV, Phys. Rev. C **88**, 014904 (2013).

[68] J. Liu, C. Shen, and U. Heinz, Pre-equilibrium evolution effects on heavy-ion collision observables, Phys. Rev. C **91**, 064906 (2015); **92**, 049904(E) (2015).